IEEE Access
Multidisciplinary | Rapid Review | Open Access Journal

Received 5 June 2023, accepted 26 June 2023, date of publication 30 June 2023, date of current version 7 July 2023.

Digital Object Identifier 10.1109/ACCESS.2023.3291143

APPLIED RESEARCH

Ground Reflection-Based Misalignment Detection of Automotive Radar Sensors

CHANUL PARK, (Graduate Student Member, IEEE), AND SEONGWOOK LEE, (Member, IEEE)
School of Electrical and Electronics Engineering, College of ICT Engineering, Chung-Ang University, Dongjak-gu, Seoul 06974, Republic of Korea

Corresponding author: Seongwook Lee (seongwooklee@cau.ac.kr)

This work was supported by the Technology Development Program funded by the Ministry of Small and Medium-Sized Enterprises (SMEs) and Startups (MSS), South Korea, under Grant S3291987.

ABSTRACT In this paper, we propose a method for detecting the misalignment of automotive radar sensors. Ensuring the accurate operation of automotive radar sensors is essential for the safety of drivers and passengers. However, when radar sensors are misaligned, they may perceive the surrounding road environment inaccurately, providing incorrect information to the vehicle's control systems. This can lead to erroneous decisions and potentially cause traffic accidents. Therefore, a method of examining the alignment state of the automotive radar sensors is required. Furthermore, due to the time-consuming and expensive nature of removing the bumper to access the radar sensor for direct inspection, an alternative method of detecting misalignment indirectly is necessary. Our method enables the detection of misalignment in automotive radar sensors through the utilization of ground reflections of radar signals. Depending on the mounting angle of the radar sensor, the range-Doppler (RD) map generated from the received signal reflected from the ground varies significantly. This RD map can be used to classify the mounting angle of the radar sensor to detect the misalignment. We design a convolutional neural network (CNN)-based classifier with the RD map as input. Using the CNN-based classifier, we estimated the mounting angle of the radar sensor with an average accuracy of 94.72%, demonstrating that our proposed method can detect the misalignment of the radar sensor effectively.

INDEX TERMS Automotive radar, ground reflection, misalignment.

I. INTRODUCTION

In recent years, the demand for advanced driver assistance systems (ADAS) or autonomous driving technologies had increased significantly, leading to the development and implementation of various sensors in the automotive industry. These sensors include vision sensors, lidar sensors, and radar sensors, which are used for ADAS functions such as lane departure warning [1], [2], adaptive cruise control [3], [4], blind-spot detection [5], [6], and autonomous emergency braking [7], [8]. Among these sensors, radar sensors have demonstrated reliable and efficient performance, regardless of weather or poor lighting conditions [9]. In addition, due to the radar sensor's ability to penetrate certain materials, automotive radar sensors are commonly mounted behind bumpers or grilles [10]. This placement ensures that the radar sensors operate effectively without affecting vehicle's aerodynamic performance or aesthetic appearance. However, concealed placement of radar sensors may cause problems if external shocks or loosening of fasteners while driving distort the sensors' initial mounting position. The misalignment of the radar sensors can affect their performance, such as incorrect estimation of a target's range, relative velocity, and angle, which poses serious threat to the safety of drivers and passengers. Nevertheless, because the concealed placement makes the visual inspection of the radar sensors difficult, it is hard to identify any issues with the radar sensors' mounting position. Removing the bumpers or grilles may be necessary to inspect the sensor, but this can be a time-consuming and expensive process. Therefore, several methods have been developed to indirectly detect misalignment of the radar sensor without disassembling the vehicle.

The associate editor coordinating the review of this manuscript and approving it for publication was Julien Le Kernec.

For example, Rohde & Schwarz has developed the R&S ®QAR automotive radome tester, a millimeter-wave imaging system that can verify the mounting position of a radar sensor behind the bumper [11]. In addition, DAS 3000 manufactured by Bosch detects misalignment angles of the radar sensor by installing a calibrated target, such as metal reflector, at a predefined distance in front of the radar [12]. However, conventional methods or devices are typically designed to be used for end-of-line testing in a manufacturing facility or for a re-calibration process at a repair facility after a bumper is reinstalled, rather than for a real-time detection on the road. Therefore, a detection method is necessary to warn the driver when the alignment of the automotive radar sensor is compromised. Studies focusing on detecting the misalignment of the automotive radar sensor on the road have not been intensively conducted. The authors in [13] proposed a method for estimating the mounting angle of the frequency-modulated continuous wave (FMCW) radar sensor based on the features such as mean, variance, coefficient of variance, kurtosis, skewness, and maximum value of signals, which are reflected from the target vehicle, in the frequency domain. Then, they used k-nearest neighbor (k-NN) algorithm to classify the set of features. Based on this classification, they estimated the mounting angle of the radar sensor. However, the proposed method in [13] may have limitations when applied to different types of target vehicles. To verify the effectiveness of the method for different types of vehicles, it is necessary to collect and analyze data from multiple types of vehicles, which can be a time-consuming process.

This paper proposes a method for detecting the misalignment of FMCW automotive radar sensors in elevation direction using a convolutional neural network (CNN)-based classifier. The proposed method involves using changes in the range-Doppler (RD) map of the signal reflected from the ground that arise from different mounting angles of the radar sensor. First, we mount an FMCW radar sensor operating at 77 GHz onto a moving platform at a height of 0.55 m above the ground. This height corresponds to the typical height of a bumper or grille, in which automotive radar sensors are usually mounted. During the measurements, we simulate the misalignment of the radar sensor by adjusting the mounting angle of the radar sensor. Specifically, we vary the elevation angle of the radar sensor at an interval of 10°, from −40° to 40°. We then generate two-dimensional (2-D) RD maps by applying the 2-D fast Fourier transform (FFT) to the obtained radar signals. In an automotive FMCW radar sensor, the RD map consists of peaks corresponding to the targets, and the amplitude of the peak varies significantly depending on the mounting angle of the radar sensor. Therefore, the mounting angle of the radar sensor can be estimated by analyzing the RD map. To enable seamless detection of misalignment of the radar sensor, we extract the specific region of the RD map corresponding to the ground reflection. Consequently, our proposed method can operate regardless of the presence of other vehicles, as it utilizes the signal reflected from the ground in close proximity of the ego-vehicle.

Finally, we design a CNN-based classifier to classify generated RD maps and detect any changes to the mounting angle of the radar sensor. The CNN is widely used in the field of radar signal processing, especially for the application of radar spectrograms [14], [15], [16], [17]. For instance, the authors in [14] used a deep CNN to classify different hand gestures based on the Doppler-time maps as input. In [15], the authors classified the modulation types of interference signals in automotive FMCW radar sensors using a CNN-based classifier that receives RD maps as input. In addition, in [16], a method for identifying different human motions with the CNN-based classifier trained with cropped range-time maps was proposed. Moreover, a CNN-based classifier with range-angle maps as input was used to estimate the instantaneous heading direction of a vehicle in [17]. In this paper, we train the CNN-based classifier with generated RD maps and test its performance. By using the CNN-based classifier, mounting angles of the radar sensor are estimated with an average accuracy of 94.72%. We believe that our proposed method can estimate the mounting angle of the radar sensor in elevation direction, allowing for real-time detection of misalignment in automotive radar sensors on the road.

The main contributions of this paper can be summarized as follows:

- We propose a method for detection of misalignment in automotive radar sensors using a CNN-based classifier, which eliminates the need for drivers to visit a specific facility to inspect the mounting status of the radar sensor.
- Our proposed method uses the CNN to detect the misalignment of the radar sensor. Compared with the previous study [13], our method does not require a complicated feature extraction and only the RD map is used as input.
- In addition, our method uses the 2-D FFT for processing the radar signals which are already present in the conventional automotive radar system. Therefore, it does not required any alteration to the existing automotive radar system, and only the pre-trained classifier needs to be added inside the vehicle for the detection of misalignment.

The remainder of the paper is organized as follows. In Section II, we describe the basics of the fast chirp FMCW radar sensor. Then, in Section III, the environment for the radar signal measurement and the results of the signal processing is presented. Next, our proposed CNN-based classifier and its classification performance are described in Section IV. Finally, we conclude this paper in Section V.

II. BASICS OF AUTOMOTIVE FMCW RADAR SENSOR

A. FAST CHIRP FMCW RADAR SIGNAL MODEL

In this section, we describe the basics of fast chirp FMCW radar signals. The FMCW radar sensor transmits a signal of which the frequency changes linearly over time. The transmitted signal of the FMCW radar sensor can be

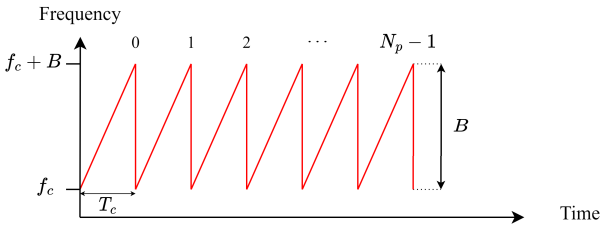

FIGURE 1. Transmitted waveform of the fast chirp FMCW radar sensor.

expressed as

$$s_t(t) = A_t \exp\left[j2\pi\left\{f_c t + \frac{B}{2T_c}t^2\right\}\right] (0 \le t \le T_c), \quad (1)$$

where A_t, f_c, B, and T_c denote the amplitude, carrier frequency, bandwidth, and chirp sweep time, respectively. When the transmitted signal $s_t(t)$ is reflected from M targets, the received signal $s_r(t)$ can be expressed as

$$s_r(t) = \sum_{m=1}^{M} A_{r_m} \exp\left\{j2\pi(f_c + f_{d_m})(t - t_{0_m}) + \pi\frac{B}{T_c} \times (t - t_{0_m})^2\right\} \left(\min_m t_{0_m} \le t \le T_c + \max_m t_{0_m}\right), \quad (2)$$

where A_{r_m} denotes the amplitude of the signal reflected from the m-th target, t_{0_m} denotes the time delay caused by the range between the m-th target and the radar, and f_{d_m} denotes the Doppler frequency caused by the relative velocity of the m-th target, respectively. Furthermore, t_{0_m} and f_{d_m} can be expressed as $\frac{2R_m}{c}$ and $\frac{2f_c v_m}{c}$, where R_m and v_m denote the range and relative velocity of the m-th target, respectively. Then, the received signal $s_r(t)$ is multiplied with the transmitted signal $s_t(t)$ in the frequency mixer. In addition, the output of the mixer is passed through the low pass filter where the high frequency component of the signal is filtered (i.e., removed). The resulting baseband signal can be expressed as

$$s(t) = \sum_{m=1}^{M} \frac{A_t A_{r_m}}{2} \exp\left[j2\pi\left\{\left(\frac{2BR_m}{T_c c} + \frac{2f_c v_m}{c}\right)t + \frac{2f_c R_m}{c}\right\}\right] \left(\max_m t_{0_m} \le t \le T_c\right). \quad (3)$$

Next, the baseband signal is converted into a discrete signal through a sampling process in an analog-to-digital converter (ADC), which can be expressed as

$$s[n] = \sum_{m=1}^{M} \frac{A_t A_{r_m}}{2} \exp\left[j2\pi\left\{\left(\frac{2BR_m}{T_c c} + \frac{2f_c v_m}{c}\right)\frac{n}{f_s} + \frac{2f_c R_m}{c}\right\}\right] (n = 0,\ 1,\ \cdots,\ N_s - 1), \quad (4)$$

where n, f_s, and N_s denote the ADC sample index, ADC sampling frequency, and the number of ADC samples per chirp, respectively. In fast chirp FMCW radar sensors, multiple chirps with short chirp sweep time are transmitted, as shown in Fig. 1.

Therefore, considering the short chirp sweep time and the phase difference between each chirp, the discrete baseband signal can be modified as

$$s[n,\ p] = \sum_{m=1}^{M} \frac{A_t A_{r_m}}{2} \exp\left[j2\pi\left\{\frac{2BR_m}{T_c c}\frac{n}{f_s} + \frac{2f_c v_m}{c}pT_c + \frac{2f_c R_m}{c}\right\}\right] (p = 0,\ 1,\ \cdots,\ N_p - 1), \quad (5)$$

where N_p and p denote the total number of chirps and chirp index, respectively. The signal $s[n,\ p]$, i.e., beat signal, contains information regarding the range and relative velocity of the target in its frequencies. Therefore, the 2-D FFT is applied in the digital signal processor to the beat signal, which can be expressed as

$$S[k,\ q] = \sum_{n=0}^{N_s-1}\sum_{p=0}^{N_p-1} s[n,\ p] \exp\left(-j2\pi\left(\frac{kn}{N_k} + \frac{qp}{N_q}\right)\right), \quad (6)$$

where k ($k = 0,\ 1,\ \cdots,\ N_k - 1$) and q ($q = 0,\ 1,\ \ldots,\ N_q - 1$) denote the indices in frequency domain. In addition, N_k and N_q denote number of FFT points. From the magnitude response of $S[k,\ q]$, we can estimate the target's range and velocity because peaks occur at the beat frequencies. Furthermore, we can convert each index in the frequency domain into corresponding values representing the range and velocity, which can be expressed as

$$R_{\text{idx}} = \frac{T_c c}{2B}k \quad (7)$$

and

$$v_{\text{idx}} = \frac{c}{2f_c}q, \quad (8)$$

because T_c, f_c, B, c, and T_s are fixed in the radar system. Thus, the magnitude of $S[k,\ q]$ is denoted as the RD map.

B. DIFFERENCES IN RECEIVED SIGNALS BASED ON MOUNTING ANGLES

In this section, we describe variations in radar signals due to different mounting angles of the radar sensor. Fig. 2 shows the illumination of radar sensor in respect to different mounting angles. In the figures, h denotes the mounting height of the radar sensor, and ϕ denotes the angle of the misalignment, i.e., mounting angle. In addition, ψ_{FOV} and θ_{FOV} denote the field of view (FOV) of the radar sensor in elevation and azimuth direction, respectively. The ground inside the FOV of the radar sensor is highlighted by the red line.

In this paper, the radar signals reflected within the range of 0 m to y_0 m, which is highlighted by the blue box, are used as input by cropping the RD map, which will be further described in Section IV-A. The magnitude of the RD map is influenced by the signal amplitude of the received signal A_r, which is directly proportional to the power of the received

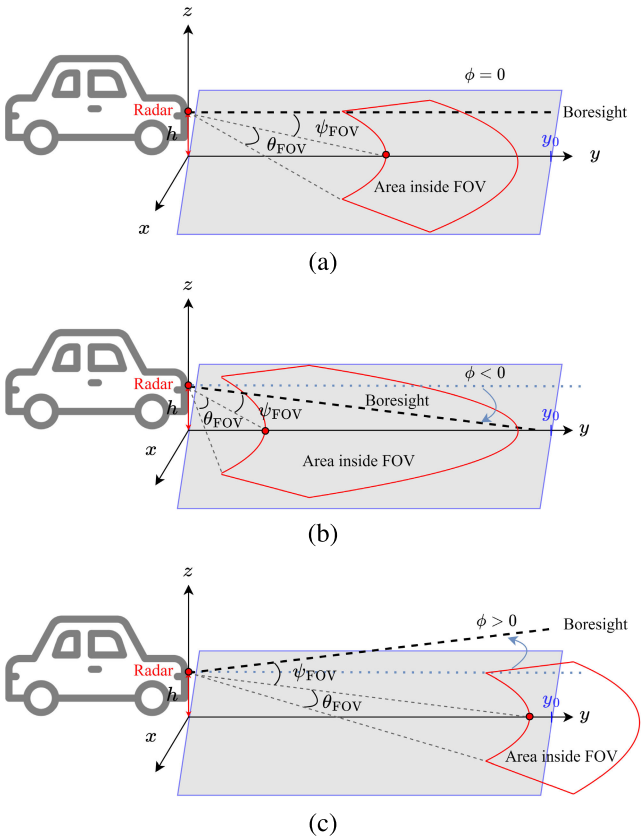

FIGURE 2. Geometry for ground reflection considering radar sensor's FOV with different mounting angle of radar sensor: (a) properly aligned ($\phi = 0$), (b) directed towards the ground ($\phi < 0$), and (c) directed towards the sky ($\phi > 0$).

signal. The received signal power can be expressed by the radar equation [18], which is given as

$$P_r = \frac{P_t G^2 \lambda^2 \sigma_{\text{RCS}}}{(4\pi)^3 R^4}, \tag{9}$$

where P_t, G, λ, and σ_{RCS} denote the transmitted power, antenna gain, wavelength of the signal, and radar cross section (RCS), respectively. If we assume that the P_t, σ_{RCS}, and λ remain constant and considering the specified range, the power of the reflected signal depends on the antenna gain. The antenna gain is determined by the directivity of the antenna's beam pattern, which is the inherent characteristics of the antenna. The antenna gain is normally maximized in the boresight direction and attenuates as the angle deviates from it. In addition, the FOV of the radar sensor is typically defined as the angle at which the antenna gain attenuates to -10 dB relative to the boresight direction. Consequently, the power of the received signal varies depending on the mounting angle of the radar sensor. For instance, when the radar sensor is directed towards the ground, which is shown in Fig. 2 (b), the boresight will also be directed toward the ground. As a result, the received signal power will be higher compared to a scenario where the radar sensor is properly aligned, which is the case of Fig. 2 (a), because of the high antenna gain.

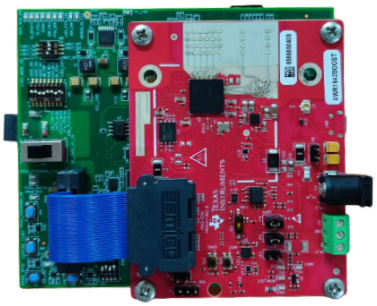

FIGURE 3. TI's AWR1642 with DCA1000 attached.

TABLE 1. Specifications of the radar sensor used in measurements.

Radar parameters	Values
Carrier frequency (f_c)	77 GHz
Bandwidth (B)	3 GHz
Number of chirps (N_p)	128
Number of ADC samples per chirp (N_s)	256
Chirp sweep time (T_c)	100 μs
ADC sampling frequency (f_s)	100 MHz
Frame time (T_f)	40 ms
Maximum unambiguous range (R_{max})	25 m
Range resolution (R_{res})	0.05 m
Maximum unambiguous velocity (V_{max})	$\pm$4.87 m/s
Velocity resolution (V_{res})	0.076 m/s
Field of view (ψ_{FOV})	-45° to 45°

Conversely, if the radar sensor is pointed towards the sky, which is shown in Fig. 2 (c), the area within the radar's FOV falls outside the range of 0 m to y_0 m and the reflection from the ground within the range of 0 m to y_0 m is substantially low due to the low antenna gain.

III. ACQUISITION AND PREPROCESSING OF RADAR SIGNAL

A. MEASUREMENT ENVIRONMENT

To validate the effectiveness of the proposed method, we conducted moving state measurements. In our measurements, we used the AWR1642BOOST radar sensor manufactured by Texas Instruments (TI), which is shown in Fig. 3. The AWR1642BOOST is connected with the DCA1000 evaluation model, that allows the user to access raw radar signals over Ethernet [19]. In addition, the AWR1642BOOST is equipped with 2 transmit antenna elements and 4 receiving antenna elements. We set the radar sensor to operate at a bandwidth of 3 GHz with a carrier frequency of 77 GHz, which is the frequency band used in conventional automotive radar sensors [20]. The radar sensor transmits 128 chirps within a frame time of 40 ms, with 256 ADC samples per chirp. A total of 200 frames are used per measurement. The chirp sweep time is set to 100 μs, and the ADC sampling frequency is 100 MHz. The specifications of the radar sensor we used in the measurements are summarized in Table 1. We conducted our measurements at a parking lot located in Bobst Hall at Chung-Ang University, which is shown in Fig. 4.

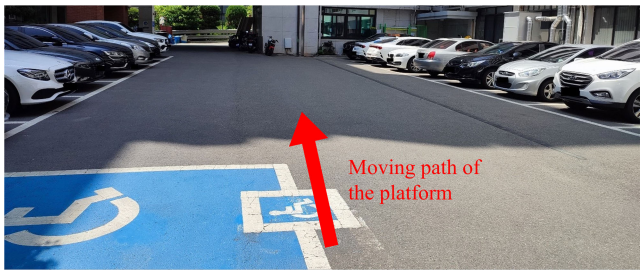

FIGURE 4. Photograph of the measurement environment.

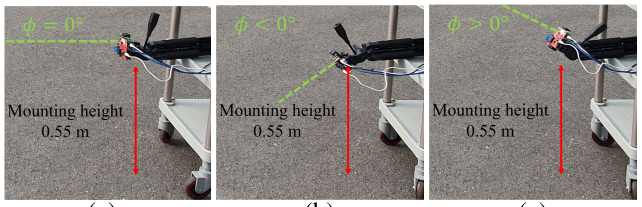

FIGURE 5. Examples of measurements with different mounting angles for radar sensor: (a) $\phi = 0$, (b) $\phi < 0$, and (c) $\phi > 0$.

In the measurements, we mounted the radar on a moving platform at a height of 0.55 m from the ground, which is the typical height of the bumper or grilles where automotive radar sensors are usually mounted. During the measurements, we moved the platform at an approximate speed of 1.4 m/s. The speed of the platform does not impact the performance of our method, as we extract the RD map specifically attributed to ground reflections in consideration of the ego-velocity, which is described in Section IV-A. We adjusted the mounting angle of the radar sensor across a range of $-40°$ to $40°$ with an interval of $10°$ to simulate the misalignment of the automotive radar sensor, resulting in radar signals obtained at 9 different mounting angles. Fig. 5 shows the examples of different mounting angles for measurements. In Fig. 5(a), the radar was properly aligned and is facing forward. Example of negative mounting angle, i.e., directed toward the ground, is shown in Fig. 5(b). In addition, Fig, 5(c) shows the case of positive mounting angle, where the radar sensor is directed toward the sky. From the measurements, we accumulated 800 RD maps for each mounting angle, resulting in a total of 7200 RD maps. Examples of RD maps obtained at different mounting angles of the radar sensor are shown in Fig. 6. In Fig. 6(a), other targets (e.g., parked vehicles) along with the ground reflection are visible. In the case of negative mounting angle, which is shown in Figure 6(b), only the ground reflection is dominant in the RD map. Conversely, overall strength of reflected signals decreased and the ground reflection is very weak in the RD map when the mounting angle of the radar sensor was positive (e.g., 40°), which is shown in Fig. 6(c).

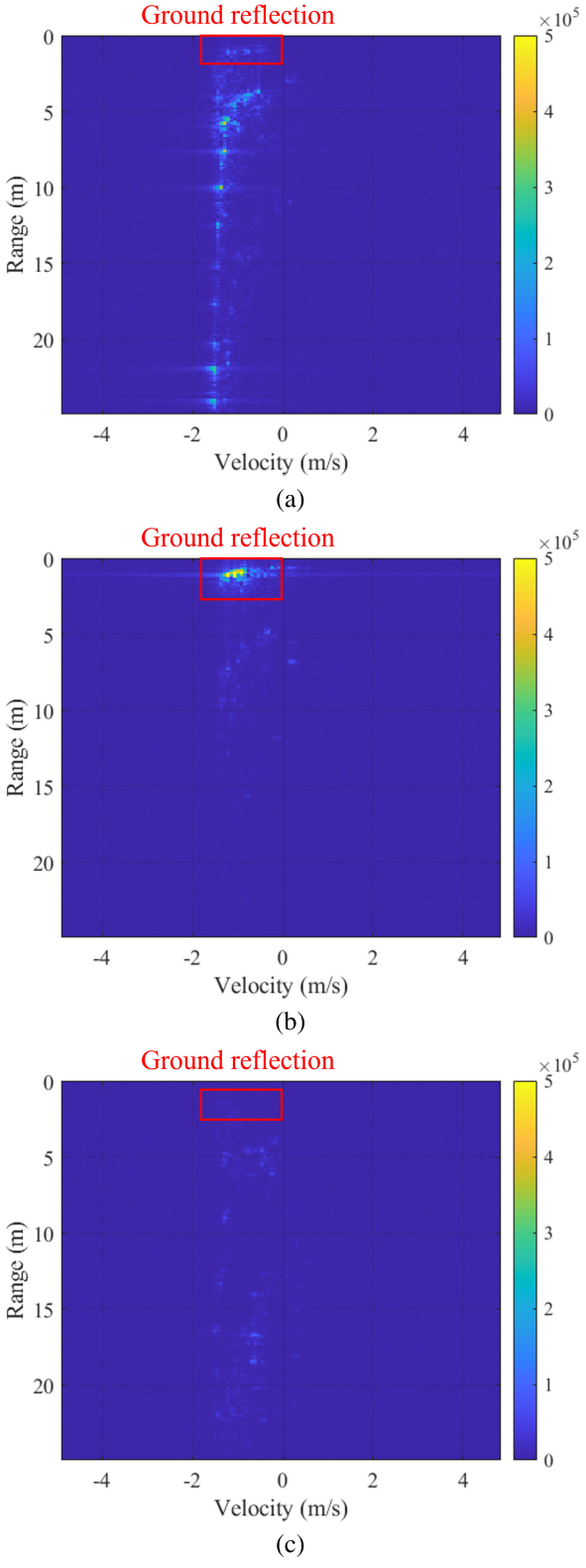

FIGURE 6. Examples of RD maps obtained at different mounting angles: (a) $\phi = 0$, (b) $\phi < 0$, and (c) $\phi > 0$.

IV. CLASSIFICATION USING CNN-BASED CLASSIFIER

A. DESIGNING INPUT FOR CNN

In this section, we describe how to change the obtained RD map into the appropriate input for the proposed CNN-base classifier. First, we obtain the RD map by applying the 2-D FFT to the obtained beat signal. However, we do not use the entire RD map $|S[k, q]|$ with a size of $N_k \times N_q$ as input to the CNN-based classifier. This is because

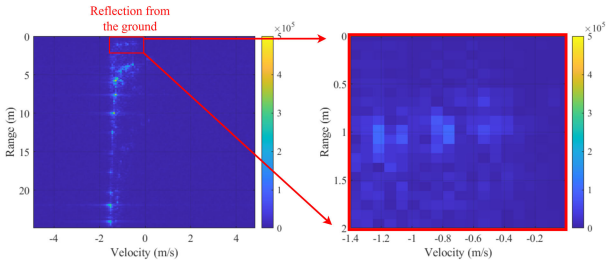

FIGURE 7. Generating input image by cropping the RD map.

we need to isolate the ground reflection in the RD map. If we were to use the entire RD map as input, the reflection from other targets on the road may also be included in the input, which is unnecessary in our method. Therefore, to ensure that our method accurately estimates the mounting angle of the radar sensor by analyzing only the ground reflection in the RD map, we crop the RD map and exclude other targets. Specifically, we focus on the region within the RD map where ground reflection is dominant, whereas the likelihood of other targets is minimized. First, we consider the mounting height and FOV of the radar sensor and crop each RD map from 0 m to 2 m, i.e., $y_0 = 2$ m.

In addition to cropping the RD map along the range-axis, it is also necessary to crop along the velocity-axis. The reason for this is that the region within the RD map caused by the ground reflection varies with the relative velocity of the ground clutter, which is in turn influenced by the velocity of the ego-vehicle. The process of determining the appropriate region to crop in terms of velocity-axis is as follows. First, we consider the maximum operating velocity $V_{\max}$ that can be measured using the radar sensor. Next, we calculate the maximum and minimum relative velocity of the ground within the properly aligned sensor's FOV. Assuming the ego-vehicle is moving at a velocity of $V_{\max}$, two values can be calculated as $-V_{\max}$ and $-V_{\max}\cos(\psi_{\text{FOV}})$, respectively [21]. Then, the absolute difference between two values is the size of cropped RD map along the velocity-axis. For example, $V_{\max}$ and ψ_{FOV} of the radar sensor used in this paper is 4.87 m/s and 45°, as shown in Table 1. Therefore, when the platform is moved at a velocity of v m/s during the measurements, the obtained RD map is cropped from $-v$ m/s to $-v + 1.4$ m/s. This cropping method allows us to maintain a fixed size of matrix data, i.e., RD maps, irrespective of the ego-velocity.

In this paper, we get 20 values on the both the range-axis and velocity-axis based on the size of range bin and velocity bin. In other words, we extract matrix data of size 20×20 and only the RD map corresponding to the ground reflection from the close proximity of the ego-vehicle is used as input. Subsequently, each cropped RD map is transformed into a 20×20 pixel portable network graphic image. Fig. 7 shows the example of cropping the RD map obtained from the measurement when the platform was moved at approximately 1.4 m/s, and the mounting angle of the radar sensor was 0°. As shown in the figure, we extracted only the region of ground reflection by cropping RD map between [0 m, 2 m] and [−1.4 m/s, 0 m/s], which is highlighted by red box. As a result, the classifier can estimate the mounting angle of the radar sensor by analyzing only the reflection from the ground. We believe this method of extracting only the ground reflection in close proximity still holds when applied to the radar sensors with relatively low elevation FOV. This is because while weak, there are signals reflected from the ground in the vehicle's proximity. In addition, whereas we only considered the misalignment in elevation angle, we believe we can also detect the misalignment in azimuth direction by using this cropping method. This is because the mounting angle of the radar sensor in azimuth direction will impact the estimated relative velocity of the ground, and therefore change the overall locations of the peaks. However, due to the structure of the proposed CNN-based classifier described in the next section, which employed the max-pooling layer, the spatial information is lost. Therefore, the detection of misalignment in azimuth direction is limited. The cropped RD maps for various mounting angles of the radar sensor, which are used for the inputs for the CNN, are shown in Fig. 8, where the size of the RD map along the velocity-axis has been extended to clearly show the differences.

B. STRUCTURE OF THE PROPOSED CNN-BASED CLASSIFIER

In this paper, we use the CNN to estimate the mounting angle of the radar sensor by classifying the RD map. The CNN is primarily composed of convolutional layers, activation layers, and the pooling layers. The convolutional layers apply a set of filters to the input data, convolving the input and producing a set of output values, which can be expressed as

$$\mathbf{Y} = f(\mathbf{X} * \mathbf{W} + \mathbf{b}), \tag{10}$$

where $\mathbf{X}$, $\mathbf{W}$, and $\mathbf{b}$ denote the input, filter weight, and filter bias, respectively, In addition, f denotes the activation function. These output values are normalized using the batch normalization layer, which improve the training speed by preventing the gradient vanishing or exploding problem as well as reducing the risk of overfitting [22]. Then, the rectified linear unit (ReLU) layer is used to provide the non-linearity to the network, which can be expressed as

$$\max(0,\, k^l) = \begin{cases} k^l, & k^l > 0, \\ 0, & \text{else}, \end{cases} \tag{11}$$

where k^l denotes the outputs of the l-th convolutional layer. Next, max pooling is performed to downsample the output of the previous layer, which helps prevent overfitting. Fig. 9 shows the example of applying the max pooling operation.

The process of convolution and max pooling is repeated multiple times in the CNN. Finally, the classification is performed using a fully connected (FC) layer and a softmax layer. The softmax layer converts the output of the FC layer in to a probability distribution over a set of classes. If we denote the input vector to the softmax layer as $\mathbf{u} = [u_1, u_2, \cdots, u_z]$ and the number of classes as Z, the output of the softmax layer

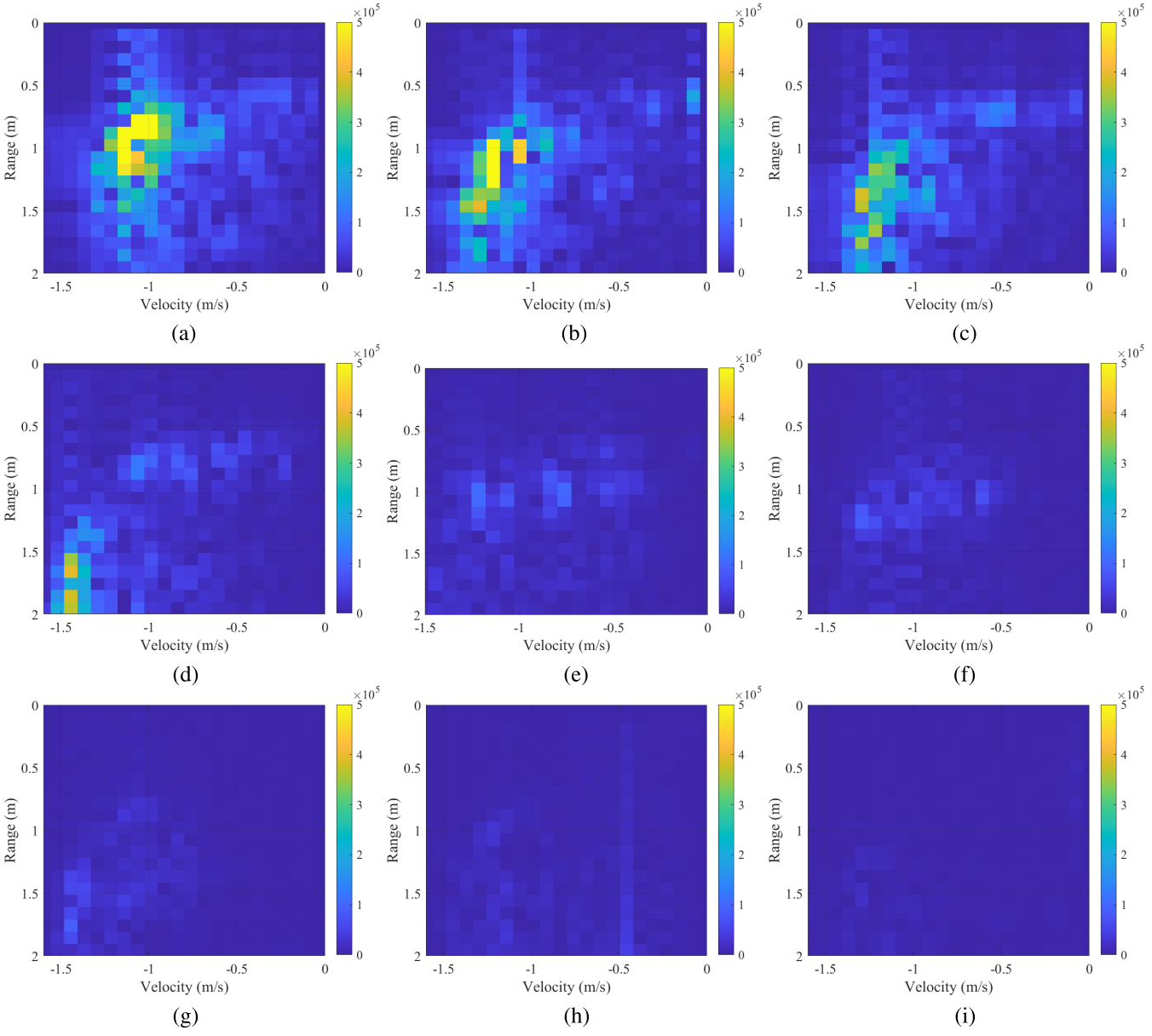

FIGURE 8. Cropped RD map used as input when the mounting angle of the radar sensor is: (a) −40°, (b) −30°, (c) −20°, (d) −10°, (e) 0°, (f) 10°, (g) 20°, (h) 30°, and (i) 40°.

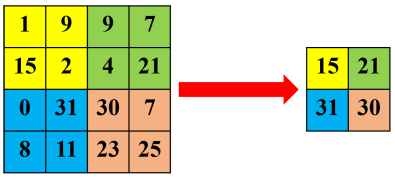

FIGURE 9. Example of max pooling with a pooling size of 2 × 2 and a stride of 2.

can be expressed as

$$\hat{\mathbf{D}} = \left[\frac{e^{u_1}}{\sum_{z=1}^{Z} e^{u_z}}, \frac{e^{u_2}}{\sum_{z=1}^{Z} e^{u_z}}, \cdots, \frac{e^{u_Z}}{\sum_{z=1}^{Z} e^{u_z}} \right], \tag{12}$$

where each element of the output vector $\hat{\mathbf{D}}$ represents the probability of the input belonging to the corresponding z-th class. By using the softmax layer, each element in the input vector is normalized to be within the range of 0 to 1, and the sum of the elements is always equal to 1. Then, based on the probabilities output by the softmax layer, class of the input is estimated as the class with the highest probability value. The filter parameters are trained by updating them through backpropagation with a gradient descent algorithm as a training algorithm. During training, the gradients of the loss function with respect to the filter parameters are computed using the training set. These gradients are used to adjust the parameters in the direction that minimizes the loss function, which is commonly computed using the cross-entropy.

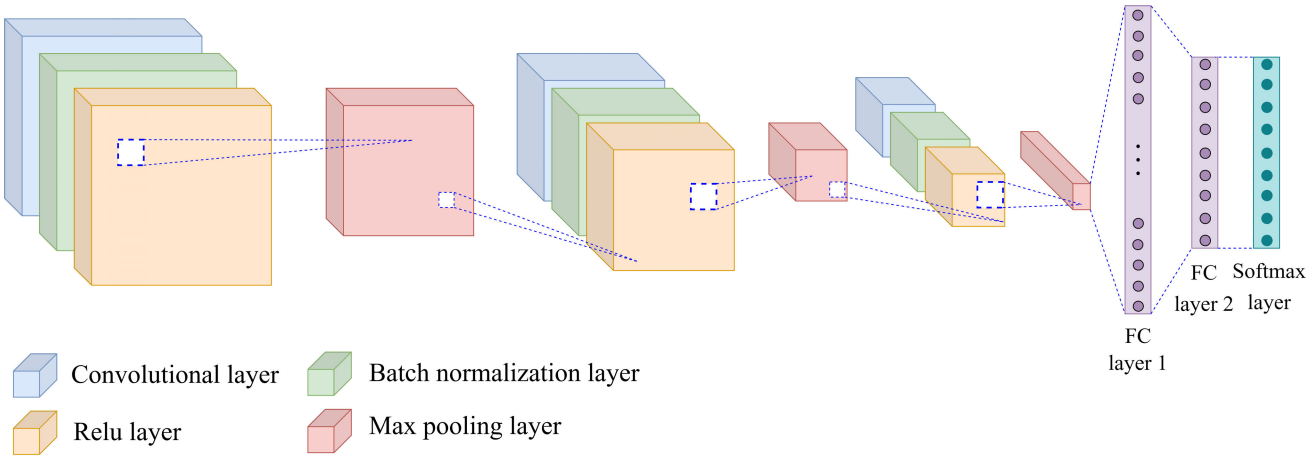

FIGURE 10. Structure of the CNN model used in our method.

Then, the filter parameters are updated by calculating the derivative of $\mathcal{L}$ with respect to $\mathbf{W}$ for each iteration, which can be expressed as

$$\mathbf{W_{i+1}} = \mathbf{W_i} - \eta \frac{\partial \mathcal{L}}{\partial \mathbf{W}}, \tag{13}$$

where η denotes the learning rate that determines the step size at each iteration.

The process of updating the filter parameters is repeated multiple times (i.e., iterations) until the optimal parameters are found which minimize the loss function. The structure of the CNN used in this paper is shown in Fig. 10. We used 3 convolutional layers, each connected by a batch normalization layer, Relu layer, and max pooling layer. All convolutional layers have the same kernel size of 3×3 and a stride of 1, but differ in the number of kernels. The number of kernels for each convolutional layer is 8, 16, and 32, respectively. The output of the convolutional layer, i.e., feature map, is passed through a batch normalization layer and Relu layer. Then, the max pooling is performed in the max pooling layer, each with a size of 2×2 and a stride of 2. Therefore, the width and height of the feature map is reduced by half, while the depth stays unchanged. After the sequence of convolutional layers and max pooling layers, the network is further connected to 2 FC layers. The first FC layer has 128 channels and the second FC layer had 9 channels, corresponding to the 9 different mounting angle of the radar sensor. Finally, the classification is made using the softmax layer. The specification of the CNN model used in this paper is presented in Table 2.

C. PERFORMANCE EVALUATION

As input for the CNN, we employed a dataset consisting of 7200 cropped RD map images in the portable network graphic format. Specifically, we selected 70% of the RD maps as the training set, 15% of as the validation set, and the remaining 15% as the test set, respectively. Each set was equally selected from the nine cases of different mounting angles of the radar sensor. The training set is used to train the CNN model using the backward propagation. The validation of the model was carried out every 10 iterations to evaluate the accuracy and reliability of the model's performance using the validation set. Finally, the test set is used to test the performance of the trained model. During the training process of the CNN model, the learning rate was set to 0.001. The batch size was set to 140, so the training data were divided into $\frac{5040}{140} = 36$ batches, and the number of epochs were set to 5, which makes the total number of iterations to $36 \times 5 = 180$. In addition, Adam, which is variant of the gradient-descent method, was used as an optimizer to update the filter parameters [23]. The CNN model was trained and tested using the MATLAB R2023a software on a computer equipped with an Intel® Core™ i5–11600K @ 3.90GHz, 16 GB of RAM, and an NVIDIA GeForce RTX 4080.

TABLE 2. Detailed specification of the CNN model.

Type of layer	Size of kernel	Number of kernels	Stride	Size of output
Conv. layer 1	3×3	8	1	$20 \times 20 \times 8$
Batch norm. layer 1	–	–	–	$20 \times 20 \times 8$
Relu layer 1	–	–	–	$20 \times 20 \times 8$
Max pool. layer 1	2×2	–	2	$10 \times 10 \times 8$
Conv. layer 2	3×2	16	1	$10 \times 10 \times 16$
Batch norm. layer 2	–	–	–	$10 \times 10 \times 16$
Relu layer 2	–	–	–	$10 \times 10 \times 16$
Max pool. layer 2	2×2	–	2	$5 \times 5 \times 16$
Conv. layer 3	3×3	32	1	$5 \times 5 \times 32$
Batch norm. layer 3	–	–	–	$5 \times 5 \times 32$
Relu layer 3	–	–	–	$5 \times 5 \times 32$
Max pool. layer 3	2×2	–	2	$2 \times 2 \times 32$
FC layer 1	–	–	–	$1 \times 1 \times 128$
FC layer 2	–	–	–	$1 \times 1 \times 9$
Softmax layer	–	–	–	$1 \times 1 \times 9$

Fig. 11 shows the classification accuracy and loss function according to the number of iterations when the Adam optimizer was used on training set and validation set. As shown in the figure, the model's performance on the validation set exhibit relatively lower classification accuracy and higher loss function compared to the training set because the validation set is not used in the training. Nevertheless,

TABLE 3. Classification results using the CNN-based classifier.

Actual angle	Estimated Angle								
	-40°	-30°	-20°	-10°	0°	10°	20°	30°	40°
-40 °	100%	0 %	0%	0%	0%	0%	0%	0%	0%
-30 °	0%	100%	0%	0%	0%	0%	0%	0%	0%
-20 °	0%	0%	100%	0%	0%	0%	0%	0%	0%
-10 °	0%	0%	0%	100%	0%	0%	0%	0%	0%
0 °	0%	0%	0%	0%	100%	0%	0%	0%	0%
10 °	0%	0%	0%	0%	7.5%	92.5%	0%	0%	0%
20 °	0%	0%	0%	0%	0%	7.5%	92.5%	0%	0%
30 °	0%	0%	0%	0%	0%	0%	25.83%	74.17%	0%
40 °	0%	0%	0%	0%	0%	0%	0%	6.67%	93.33%

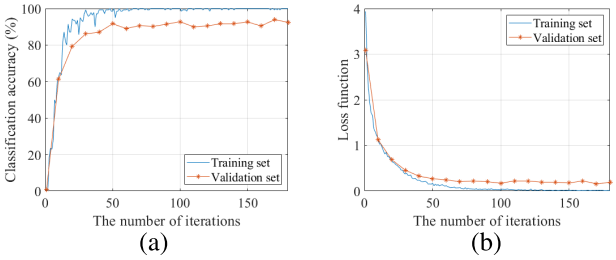

FIGURE 11. Performance of CNN model on training set and validation set in respect to the number of iterations: (a) classification accuracy and (b) loss function.

both the classification accuracy and loss function from the training set and validation set demonstrated a similar trend throughout the iterations. This indicates that the model is not solely optimized for the training data, indicating its potential to generalize effectively beyond the training set. There was no significant improvement in the performance of the model after 50 iterations, where the classification accuracy for the training set and validation set was 100% and 91.67%. In addition, the confusion matrix for the result of classification for the test set is presented in Table 3. In the table, the elements on the diagonal represent the correct classifications, while the elements off the diagonal correspond to misclassification. The classification accuracy for each mounting angle of the radar sensor was 100%, 100%, 100%, 100%, 100%, 92.5%, 92.5%, 74.17%, and 93.34%, respectively. The average classification accuracy was 94.72% and the overall classification accuracy of our method was 94.63%. For the case of $-40°$ to $-10°$ (i.e., negative mounting angle), and 0°, our method showed high classification accuracy of 100%, because, as the radar sensor tilts toward the ground, the amplitude of the signals reflected from the ground increases, making the distinction between each RD map easier. On the other hand, the classification accuracy was around 90% for the case of 10° to 40° (i.e., positive mounting angle), in addition to the 74.17% when the mounting angle was 30°. The difficulty in classifying images of RD maps for positive mounting angle arises due to the substantial decrease in signal amplitude. However, the spatial information, i.e., the location of the strongest peak in the RD map, was found to be influential in the classification. Consequently, misclassifications were limited to adjacent mounting angle.

In addition, when we removed max pooling layers from our CNN model to preserve the spatial information in the RD map, the overall classification accuracy increased to 97.96%, accompanied by a 16.67%p increase for the case of 30° mounting angle. However, the exclusion of pooling layers may lead to increased computational load and may make it challenging to apply the method to other radar sensors with different range resolutions. Furthermore, we tested the performance of the model by replacing FC layer 1 to global average pooling layer, which is known to effectively replace FC layer while reducing the computational load [24]. The resulting classification accuracy was 99.17%, 100%, 99.17%, 100%, 100%, 98.33%, 100%, 45.83%, and 95.83%, respectively. The usage of global average pooling layer showed better performance for most cases. However, the classification accuracy decreased to 45.83% for the case of a 30°, where the remaining 54.17% was classified as 20°. Therefore, to compromised between classification performance and computational complexity, we chose to use both the max pooling layers and FC layer.

Finally, we compared the performance of our method with other classification algorithms: decision tree, support vector machine (SVM) and k-NN algorithm. A decision tree is a simple classification algorithm that uses a hierarchical structure composed of classification rules that determine the class of objects from its values of the features [25]. In addition, an SVM is a classification technique that aims to find a linear decision surface capable effectively separating different classes within input data mapped to a high dimension feature space [26]. Moreover, a k-NN is a non-parametric classification technique that determines the class of an input based on the classes of its k nearest neighbors in the feature space, assigning the most frequent class among the k neighbors as the predicted class for the input [27]. For the parameters of k-NN, we set the number of neighbors to 150 and employed the inverse square-distance weighting scheme, along with the use of Euclidean distances. Then, we extracted features such as mean, variance, coefficient of variance, kurtosis, skewness, and maximum value of the matrix corresponding to the cropped RD map [13]. Extracting features of radar signals is widely used in target classification [28]. We employed this method to generate appropriate input for these other classification methods, because these methods are not designed to directly handle

TABLE 4. Comparison of the average classification performance to other algorithms.

Classification method	Average classification accuracy
Proposed method	94.72%
Linear SVM with features proposed in [13]	82.13%
k-NN with features proposed in [13]	78.70%
Decision tree with features proposed in [13]	75.83%

image format data. The average classification performance for each algorithm is presented in Table 4. The decision tree showed a low classification accuracy because of its inadequacy in handling high-order data. The k-NN also showed a low classification accuracy. While the performance of SVM exhibited a higher accuracy compared to the decision tree or k-NN, its accuracy is still considered insufficient. These low accuracies of other algorithms are attributed to misclassifications to adjacent mounting angles, rather than completely different mounting angles. Therefore, our proposed CNN-based classifier demonstrated to be most effective among the alternatives, surpassing all other classification methods.

V. CONCLUSION

In this paper, we proposed a method for detecting the misalignment of automotive radar sensors using a CNN-based classifier. We mounted the radar sensor operating at 77 GHz on a moving platform and adjusted the mounting angle of the radar sensor from $-40°$ to $40°$ at intervals of $10°$ to simulate the misalignment of the automotive radar sensor. We then generated RD maps by applying the 2-D FFT to the obtained radar signals. From the generated RD maps, we identified variations in the RD maps corresponding to signals reflected from the ground, which were dependent on the mounting angle of the radar sensor. In addition, to accurately estimates the mounting angle of the radar sensor by analyzing only the ground reflection, we cropped the RD maps considering the specification of our radar sensor. For classification of these cropped RD maps, we designed a CNN-based classifier. With the designed CNN-based classifier, we estimated the mounting angle of the radar sensor with an average accuracy of 94.72%. Furthermore, we compared the classification performance of our method with other classification techniques, and the results demonstrated that our method achieved superior classification accuracy. We hope that our proposed method can be used to detect the misalignment of automotive radar sensors in real-time on the road, enabling warnings to drivers about the state of their radar sensors.

REFERENCES

[1] B. Benligiray, C. Topal, and C. Akinlar, "Video-based lane detection using a fast vanishing point estimation method," in *Proc. IEEE Int. Symp. Multimedia*, Irvine, CA, USA, Dec. 2012, pp. 348–351.

[2] Z. Feng, M. Li, M. Stolz, M. Kunert, and W. Wiesbeck, "Lane detection with a high-resolution automotive radar by introducing a new type of road marking," *IEEE Trans. Intell. Transp. Syst.*, vol. 20, no. 7, pp. 2430–2447, Jul. 2019.

[3] H. S. Park, D. J. Kim, C. M. Kang, S. C. Kee, and C. C. Chung, "Object detection in adaptive cruise control using multi-class support vector machine," in *Proc. IEEE 20th Int. Conf. Intell. Transp. Syst. (ITSC)*, Yokohama, Japan, Oct. 2017, pp. 1–6.

[4] M. A. Bharmal and M. H. Rashid, "Designing an autonomous cruise control system using an A3 LiDAR," in *Proc. 2nd Int. Conf. Innov. Eng. Technol. (ICIET)*, Dhaka, Bangladesh, Dec. 2019, pp. 1–6.

[5] G. Liu, L. Wang, and S. Zou, "A radar-based blind spot detection and warning system for driver assistance," in *Proc. IEEE 2nd Adv. Inf. Technol., Electron. Autom. Control Conf. (IAEAC)*, Chongqing, China, Mar. 2017, pp. 2204–2208.

[6] Y. Shen and W. Q. Yan, "Blind spot monitoring using deep learning," in *Proc. Int. Conf. Image Vis. Comput. New Zealand (IVCNZ)*, Auckland, New Zealand, Nov. 2018, pp. 1–5.

[7] H. Kim and B. Song, "Vehicle recognition based on radar and vision sensor fusion for automatic emergency braking," in *Proc. 13th Int. Conf. Control, Autom. Syst. (ICCAS)*, Gwangju, South Korea, Oct. 2013, pp. 1342–1346.

[8] L. Xia, T. D. Chung, and K. A. A. Kassim, "An automobile detection algorithm development for automated emergency braking system," in *Proc. 51st ACM/EDAC/IEEE Design Autom. Conf. (DAC)*, San Francisco, CA, USA, Jun. 2014, pp. 1–6.

[9] W. D. Jones, "Keeping cars from crashing," *IEEE Spectr.*, vol. 38, no. 9, pp. 40–45, Sep. 2001.

[10] R. Searcy. *Machine Learning Takes Automotive Radar Further*. Aptiv, Ireland. Accessed: Jun. 25, 2023. [Online]. Available: https://www.aptiv.com/en/insights/article/machine-learning-takes-automotive-radar-further

[11] *R&S®QAR Quality Automotive Radome Tester*, Rohde & Schwarz, Munich, Germany. Accessed: Jun. 25, 2023. [Online]. Available: https://www.rohde-schwarz.com/us/products/test-and-measurement/radome-tester/rs-qar-quality-automotive-radome-tester_63493-553077.html

[12] *Ready Aim Calibrate*, Bosch, Gerlingen, Germany. Accessed: Jun. 25, 2023. [Online]. Available: https://www.boschdiagnostics.com/adas

[13] J. Jung, S. Lee, S. Lim, and S. Kim, "Machine learning-based estimation for tilted mounting angle of automotive radar sensor," *IEEE Sensors J.*, vol. 20, no. 6, pp. 2928–2937, Mar. 2020.

[14] Y. Kim and B. Toomajian, "Hand gesture recognition using micro-Doppler signatures with convolutional neural network," *IEEE Access*, vol. 4, pp. 7125–7130, 2016.

[15] J. Kim, S. Lee, Y. Kim, and S. Kim, "Classification of interference signal for automotive radar systems with convolutional neural network," *IEEE Access*, vol. 8, pp. 176717–176727, 2020.

[16] S.-W. Kang, M.-H. Jang, and S. Lee, "Identification of human motion using radar sensor in an indoor environment," *Sensors*, vol. 21, no. 7, p. 2305, Mar. 2021.

[17] S. Lim, J. Jung, B. Lee, S. Kim, and S. Lee, "CNN-based estimation of heading direction of vehicle using automotive radar sensor," *IET Radar, Sonar Navigat.*, vol. 15, no. 6, pp. 618–626, Apr. 2021.

[18] M. Skolnik, *Radar Handbook*, 3rd ed. New York, NY, USA: McGraw-Hill, 2008, pp. 10–13.

[19] *DCA1000EVM Data Capture Card*. Texas Instruments, Dallas, TX, USA. Accessed: Jun. 25, 2023. [Online]. Available: https://www.ti.com/tool/DCA1000EVM

[20] C. Waldschmidt, J. Hasch, and W. Menzel, "Automotive radar—From first efforts to future systems," *IEEE J. Microw.*, vol. 1, no. 1, pp. 135–148, Jan. 2021.

[21] A. Laribi, M. Hahn, J. Dickmann, and C. Waldschmidt, "A new height-estimation method using FMCW radar Doppler beam sharpening," in *Proc. 25th Eur. Signal Process. Conf. (EUSIPCO)*, Kos, Greece, Aug. 2017, pp. 1932–1396.

[22] R. Yamashita, M. Nishio, R. K. G. Do, and K. Togashi, "Convolutional neural networks: An overview and application in radiology," *Insights Imag.*, vol. 9, pp. 611–629, Jun. 2018.

[23] D. P. Kingma and J. L. Ba, "Adam: A method for stochastic optimization," in *Proc. Int. Conf. Learn. Represent.*, San Diego, CA, USA, Mar. 2015, pp. 1–15.

[24] K. Xia, J. Huang, and H. Wang, "LSTM-CNN architecture for human activity recognition," *IEEE Access*, vol. 8, pp. 56855–56866, 2020.

[25] J. R. Quinlan, "Induction of decision trees," *Mach. Learn.*, vol. 1, no. 1, pp. 81–106, Mar. 1986.

[26] C. Cortes and V. Vapnik, "Support–vector networks," *Mach. Learn.*, vol. 20, pp. 273–297, Sep. 1995.

[27] K. Taunk, S. De, S. Verma, and A. Swetapadma, "A brief review of nearest neighbor algorithm for learning and classification," in *Proc. Int. Conf. Intell. Comput. Control Syst. (ICCS)*, Madurai, India, May 2019, pp. 1255–1260.
[28] S. Lee, B. Lee, J. Lee, and S. Kim, "Statistical characteristic-based road structure recognition in automotive FMCW radar systems," *IEEE Trans. Intell. Transp. Syst.*, vol. 20, no. 7, pp. 2418–2429, Jul. 2019.

CHANUL PARK (Graduate Student Member, IEEE) received the B.S. degree in electronics and information engineering from Korea Aerospace University (KAU), Goyang-si, Gyeonggi-do, Republic of Korea, in February 2023. He is currently pursuing the M.S. degree with Chung-Ang University (CAU), Seoul, Republic of Korea. His research interests include deep learning applications for autonomous driving, such as target detection, tracking, target classification in multi-sensor systems, and radar signal processing.

SEONGWOOK LEE (Member, IEEE) received the B.S. and Ph.D. degrees in electrical and computer engineering from Seoul National University (SNU), Seoul, Republic of Korea, in February 2013 and August 2018, respectively. From September 2018 to February 2020, he was a Staff Researcher with the Machine Learning Laboratory, AI & SW Research Center, Samsung Advanced Institute of Technology (SAIT), Gyeonggi-do, Republic of Korea. Thereafter, he was as an Assistant Professor with the School of Electronics and Information Engineering, College of Engineering, Korea Aerospace University (KAU), Gyeonggi-do, from March 2020 to February 2023. Since March 2023, he has been an Assistant Professor with the School of Electrical and Electronics Engineering, College of ICT Engineering, Chung-Ang University (CAU), Seoul. He has published more than 100 papers on signal processing for radar systems. His research interests include radar signal processing techniques, such as enhanced target detection and tracking, target recognition and classification, clutter suppression and mutual interference mitigation, and artificial intelligence algorithms for radar systems.